This is a preprint, the final version is subject to change, of the American Mineralogist (MSA)
Cite as Authors (Year) Title. American Mineralogist, in press.
(DOI will not work until issue is live.) DOI: http://dx.doi.org/10.2138/am.2013.4287

Revision 2.

A time-resolved X-ray diffraction study of Cs exchange into hexagonal H-birnessite

Claire R. Fleeger[1*], Peter J. Heaney[1], Jeffrey E. Post[2]

[1]Department of Geosciences, Pennsylvania State University, University Park PA 16802, USA

[2]Department of Mineral Science, Smithsonian Institution, Washington DC 20560, USA

[*]current address: PPG Industries, 440 College Park Dr, Monroeville PA 15146, USA

Keywords: hexagonal birnessite, cesium, cation exchange, time-resolved X-ray diffraction

Submitted to *American Mineralogist*

Revision 2.

ABSTRACT

To measure the uptake of radioactive Cs in soils that are rich in Mn oxides, we applied time-resolved synchrotron X-ray diffraction (TR-XRD), inductively coupled plasma-mass spectrometry (ICP-MS), and analytical scanning electron microscopy (SEM) to determine the kinetics and mechanisms of aqueous Cs substitution in the phyllomanganate hexagonal H-birnessite at pH values ranging from 3 to 10. We observed that the rate of Cs cation exchange into hexagonal H-birnessite exhibited only a weak dependence on pH, but the total amount of Cs loading in the interlayer region increased dramatically above pH 6.5. The increase in Cs content at higher pH may be attributed to the increasingly negative charge on the Mn-O octahedral sheets and perhaps to a structural change towards triclinic symmetry with high pH. Dissolution at low pH may have inhibited Cs sequestration. Our work supports delamination-reassembly as a mechanism of cation exchange.

INTRODUCTION

Cesium-137 is a byproduct of the plutonium production process, and it is a significant contaminant during nuclear fallout, nuclear plant meltdown, and nuclear waste storage. Following the nuclear plant disasters at Chernobyl (Ukraine), and most recently, Fukushima (Japan), ^{137}Cs was distributed widely through radioactive plumes that contaminated soils and surface waters. Moreover, ^{137}Cs is a major component of the nuclear wastes monitored by the Department of Energy (DOE) at such sites as Hanford, WA, Savannah River, SC, and Oak Ridge, TN.

At the Hanford site, ^{137}Cs is responsible for roughly 40% of the radioactivity of the nuclear waste (McKinley et al. 2001; Gee et al. 2007). Hanford was a plutonium production factory from 1943 to 1991, and its high-level nuclear waste is stored in 177 underground single- and double-shell steel tanks. Approximately 3.8 million L of waste have leaked from the single-shell tanks, partly because the high alkalinity of the waste (pH 13-14) corroded the steel. The leaking solutions are concentrated in radioactive ^{137}Cs (2×10^{10} Bq/L, equivalent to 0.04 mmol/L), and they have contaminated approximately 28,300 m^3 of soil (Gee et al. 2007). Although the contaminant solutions leaking from the tanks initially are at pH 14, the pH is neutralized with increasing distance of transport as the solutions are buffered by soil minerals (Wan et al. 2004). Consequently, in order to model the migration of Cs-rich fluids, it is necessary to study Cs uptake by soil minerals over a range of pH.

Underlying the tank farm at Hanford is the Ringold Formation, which contains predominantly sand- and cobble-sized gravel with significant amounts of clay, silt, and sand (Lindsey and Gaylord 1990). These sediments are glacial-fluvial in origin and are coated in distinct iron and manganese oxides layers (Barnett et al. 2002; Fredrickson et al. 2004). These manganese oxides make up 0.4-0.93 wt% of the Ringold Formation (Barnett et al. 2002; Fredrickson et al. 2004). Despite their minor abundances, these phases play a major role in controlling heavy metal mobility. As coatings on glacial clasts at Hanford, they occur at the interface between pore solutions and the primary soil minerals. Moreover, the high cation exchange, redox, and adsorption capacities of Mn oxides are well documented (Fu et al. 1991; Violante and Pigna 2002; O'Reilly and Hochella 2003; Weaver and Hochella 2003; Negra et al. 2005; Zhao et al. 2009; Lopano et al. 2007, 2009, 2011). Hydrous manganese oxides with layer and large-tunnel structures are most frequently observed in these soils, such as the

phyllomanganates birnessite and ranciéite, and the tunneled manganite, todorokite (Taylor et al. 1964; Vaniman et al. 2002; Fredrickson et al. 2004). All of these phases occur as submicron grains with large surface areas, but birnessite is typically the most reactive (Weaver and Hochella 2003).

In this study, we have investigated the interactions of aqueous Cs with a synthetic hexagonal H-birnessite over a range of pH. Birnessite structures have been shown to exhibit either triclinic (Lanson et al. 2002; Post et al. 2002) or hexagonal (Silvester et al. 1997; Post et al. 2008) symmetry. The structure of hexagonal birnessite differs from that of triclinic birnessite in the near-absence of Mn^{3+} and the presence of Mn vacancies (□) in the octahedral sheet, resulting in the following chemical formula for H-birnessite proposed by Silvester et al. (1997): $H_{0.33}Mn^{3+}_{0.111}Mn^{2+}_{0.055}(Mn^{4+}_{0.722}Mn^{3+}_{0.111}□_{0.167})O_2$. Subsequently, a similar hexagonal structure was refined for the natural Ca-rich analog of birnessite called ranciéite (Post et al. 2008). The charge deficits incurred by the vacancies and Mn^{3+} in place of octahedral Mn^{4+} result in negatively charged sheets, which are electrostatically balanced by Mn^{2+} and possibly hydronium or various exchanged cations between the sheets.

Dyer et al. (2000) determined distribution coefficients for the exchange of ^{137}Cs into a highly crystalline synthetic Na-birnessite, and they report that the uptake decreased as the solution pH increased from 2 to 10. In contrast, Chitrakar et al. (2011) analyzed the uptake of Cs^+ by a poorly crystalline synthetic Na-birnessite from pH 2.5 to 10.5, and they observed increasing Cs^+ sequestration between pH 2.5 and 6.0 and little change between pH 6.0 and 10.5. Chitrakar et al. attribute the disparity in sequestration behavior to the differences in crystallinity, but neither paper specifies the symmetry of the birnessite starting material. To the best of our knowledge, when the symmetry is specified, all prior studies of cation exchange in the

phyllomanganate system have focused on triclinic birnessite (e.g., Golden et al. 1986b; Mikhail and Misak 1988; Al-Attar et al. 2003; Liu et al. 2007; Lopano et al. 2007; Lopano et al. 2009). However, many scientists have demonstrated that natural soils contain both triclinic and hexagonal birnessite (Webb et al. 2005; Post et al. 2008; Tan et al. 2010; Santelli et al. 2011). In light of the high selectivity that birnessite exhibits for dissolved Cs^+ (Chitrakar et al. 2011), here we report the effects of pH on Cs cation exchange into a starting material that we know is hexagonal H-birnessite.

EXPERIMENTAL METHODS

Birnessite synthesis

Triclinic Na-birnessite was initially synthesized according to the procedure described in Golden et al. (1986a). At room temperature, oxygen was bubbled (4.2 L/min) through a mixture of chilled 250 mL 5.5 *M* NaOH and 200 mL 0.5 *M* $MnCl_2$ for five hours. The precipitate was divided evenly among 12 centrifuge tubes and centrifuged. The solution was poured off and replaced with fresh DI water; after five replicate rinsing cycles, the birnessite was stored in fresh DI water until needed for experiments. For experiments, aliquots of the stored triclinic Na-birnessite were filtered through a 0.2 μm hydrophilic polypropylene membrane filter (GH Polypro, Pall) and allowed to air dry. Dry triclinic Na-birnessite (250 mg) was ground under acetone in an agate mortar to disaggregate clumps. After the acetone had fully evaporated, the powder was reacted with 250 mL 0.001 *M* HCl (pH 3) for three hours. The resultant synthetic hexagonal H-birnessite was filtered and then rinsed with 300 mL DI water, filtered again through a 0.2 μm filter, and allowed to air dry. The material was initially characterized with a

conventional sealed Mo tube source on a Rigaku II D/MAX-RAPID microdiffractometer (Materials Characterization Laboratory, Pennsylvania State University).

Synchrotron X-ray diffraction of cation exchange

Time-resolved X-ray diffraction (TR-XRD) experiments were completed at beam line 13-BM-C at the Advanced Photon Source (APS) at Argonne National Laboratory (ANL). Approximately 4 mg of hexagonal H-birnessite were packed between two cotton plugs in a 0.7 mm quartz capillary and attached to a flow-through apparatus based on the design of Wall et al. (2011). The five Cs-rich cation exchange solutions had the same initial Cs concentration of 0.001 *M,* and pH ranged from 3 to 10 (pH 3, 5, 6.5, 9, 10). The pH was adjusted with CsOH, and the Cs concentration was controlled with CsCl. Experiments were not completed at pH 13 because increasing the alkalinity using CsOH required a Cs concentration of 0.1 *M*. The solution flow rate was 1 drop/min (~ 0.05 mL/min). TR-XRD patterns were collected every 60 seconds for 5 to 9 hours using a MAR165 CCD detector at a wavelength of 0.8335 Å. The sample to collector distance was 97.6 mm, yielding a 2θ range of 4-50°. Rietveld refinements (Rietveld 1969) were completed for each TR-XRD pattern using the EXPGUI interface (Toby 2001) of the general structure analysis system (GSAS) (Larson and Von Dreele 1994). Starting structures were drawn from the model structure of hexagonal H-birnessite proposed by Lanson et al. (2000) with atom positions determined by Heaney et al. (2003). The background intensities for the TR-XRD patterns were fit using up to 15 terms of a linear interpolation function. The peak profiles were modeled by a pseudo-Voigt profile function as parameterized by Thompson et al. (1987), with asymmetry correction by Finger et al. (1994), and microstrain anisotropic broadening terms of Stephens (1999).

Revision 2.

During initial cycles of refinement only the background, scale, peak profile, and unit-cell parameters were allowed to vary. The position of the O atom in the Mn-O sheet was then refined. Following refinements of the interlayer atom positions, occupancy factors and isotropic atomic displacement factors for the interlayer sites were allowed to vary. Once the interlayer atoms were settled, the isotropic thermal parameters for the Mn and O in the octahedral sheets were refined, followed alternately with those for the interlayer atoms. The final χ^2 values for end-member hexagonal Cs-birnessite ranged from 2.76-4.82 (Table 1). As is often the case, the standard deviations calculated by GSAS for the lattice parameters are lower than the true errors, which are revealed by the scatter in the refined values as a function of temperature (Post and Bish 1989). The errors calculated by GSAS are presented in the tables and figures of this paper with the understanding that the actual errors may be more than an order of magnitude higher than the calculated deviations.

Chemical analysis of eluate

The eluate was collected as a function of time; a stepping motor controlled a UR-150 Newport Rotary Stage with an Al tray capable of supporting 15 wide-mouth 15 mL polypropylene vials. The stepping motor was programmed to rotate to the next vial every 20 min. The eluate was analyzed with an X-Series 2 Thermo Scientific quadrupole inductively coupled plasma-mass spectrometer (ICP-MS) in conjunction with Thermo Scientific PlasmaLab software (Materials Characterization Laboratory, Pennsylvania State University) to determine the change in Cs and Mn elemental concentrations.

An FEI Nova NanoSEM 600 analytical scanning electron microscope (ASEM) equipped with Thermo Fisher Scientific NSS 2.3.89 software (Mineral Sciences Analytical Laboratories,

Smithsonian Institution) was used to determine the distribution of Cs across partially exchanged hexagonal H-birnessite grains. These partially exchanged products were obtained by flowing 0.001 *M* CsCl solutions through hexagonal H-birnessite powders in capillaries for 40 min at pH 9. The birnessite was unpacked from the glass capillary, rinsed with 300 mL DI water, and allowed to air dry at room temperature. Dry samples were mounted on SEM stubs with carbon tape for elemental mapping analysis.

Kinetic analysis

We applied the approach of Lopano et al. (2011) to determine the kinetics of cation substitution into the hexagonal H-birnessite structure. This method assumes that cation exchange in this system obeys Vegard's Law, which posits that the volume of the unit cell varies linearly with the extent of cation exchange (Denton and Ashcroft 1991). As suggested in Lopano et al. (2009), this presumption is reasonable, since the large size of Cs^+ will expand the interlayer of birnessite-like phases. However, the application of Vegard's Law to birnessite is complicated by the appearance of an intermediate product, in which Cs has fully exchanged for the interlayer cation but is positionally disordered within the interlayer. The authors treated this issue by including the disordered state as a distinct phase that contributed to the overall unit-cell volume. Following Lopano et al. (2011), we propose that the measured volume of the unit cell (V_{tot}) at any point during the exchange of Cs into hexagonal H-birnessite can be represented by a summation of the three individual phase fractions (X_x), each multiplied by their respective unit-cell volumes, q, r, and s:

$$V_{tot} = qX_A + rX_B + sX_C \quad (1)$$

where X_A is the phase fraction of initial hexagonal H-birnessite, X_B is the phase fraction of disordered hexagonal Cs-birnessite, and X_C is the phase fraction of ordered hexagonal Cs-birnessite.

As shown in Lopano et al. (2011), the kinetics of Cs^+ exchange into triclinic Na-birnessite by extension can be modeled as a two-stage linear reaction. The first stage involves the complete exchange of cations, and in the second stage cations reorder within the interlayer to more thermodynamically stable positions (Fig. 1). The rate constant of each reaction stage (k_1 and k_2, respectively, with units min^{-1}) was determined according to standard kinetic equations for a first-order compound reaction (Fromherz 1964):

$$A \overset{k_1}{\rightarrow} B \overset{k_2}{\rightarrow} C \quad (2)$$

$$X_A = X_A^0 e^{-k_1 t} \quad (3)$$

$$X_B = \frac{X_A^0 k_1}{k_2 - k_1}(e^{-k_1 t} - e^{-k_2 t}) \quad (4)$$

$$X_C = X_A^0 \left\{1 - \frac{k_1 k_2}{k_2 - k_1}\left(\frac{e^{-k_1 t}}{k_1} - \frac{e^{-k_2 t}}{k_2}\right)\right\} \quad (5)$$

where t is time and X^0_A is the initial phase fraction of starting material, A. According to mass balance:

$$X_{tot} = X_A^0 = X_A + X_B + X_C = 1 \quad (6)$$

or

$$X_A^0 = 1 . \quad (7)$$

Eqns. 3-7 were substituted into Vegard's Law (Eqn. 1):

$$V_{tot} = q e^{-k_1 t} + \frac{r k_1}{k_2 - k_1}\left(e^{-k_1 t} - e^{-k_2 t}\right) + s\left\{1 - \frac{k_1 k_2}{k_2 - k_1}\left(\frac{e^{-k_1 t}}{k_1} - \frac{e^{-k_2 t}}{k_2}\right)\right\} . \quad (8)$$

Revision 2.

The dependence of volume versus time for each pH was fit with Eqn. 8 using Origin 6.1, solving for q, r, s, k_1, and k_2. These five variables were allowed to iterate simultaneously using the Levenberg-Marquardt algorithm until the reduced χ^2 was minimized. For this study, we were most interested in the initial exchange of cations when $X_A = 1$ and $t = 0$, and not the reordering of cations; therefore, the initial rate of the cation exchange was determined using the first-stage rate constant (k_1) and phase fractions X_A and X_B. The initial rate in terms of X_A, X_B, and k_1 can be defined with standard first-order reversible kinetics as (Lasaga 1981)

$$\frac{dX_A}{dt} = -k_1 X_A^{\,n} \tag{9}$$

$$\frac{dX_B}{dt} = k_1 X_A^{\,n} \tag{10}$$

where n is the reaction order. Taking the derivative of Vegard's Law (Eqn. 1) with respect to time,

$$\frac{dV}{dt} = q\frac{dX_A}{dt} + r\frac{dX_B}{dt}, \tag{11}$$

and substituting Eqn. 9 and 10 into Eqn. 11, the initial rate dV/dt in Å^3/min is

$$\lim_{t \to 0,\, X_A \to 1} \left(\frac{dV}{dt}\right) = -k_1 q + k_1 r \tag{12}$$

or

$$\frac{dV}{dt} = k_1(r - q). \tag{13}$$

When we plotted the log of the initial rate as a function of pH, we could calculate a linear regression for which the negative slope was the reaction order, n, and the y-intercept was the log of the initial rate constant, w, with units Å^3/(min·mol):

Revision 2.

$$\log\left(\frac{dV}{dt}\right) = -n(pH) + \log w \quad (14)$$

which simplifies to

$$\frac{dV}{dt} = w\left[H^+\right]^n \quad (15)$$

Thus, Eqn. 15 allows us to determine the effect of solution pH on the rate of Cs cation exchange as measured from volume changes of the hexagonal birnessite unit cell.

RESULTS

The substitution of Cs^+ into hexagonal H-birnessite is evident from X-ray diffraction patterns through a marked decrease in the ratio of the 001 to 002 diffraction peaks (Fig. 2). Cs has a considerably larger scattering factor than the exchangeable proton/water complex in the interlayer of hexagonal H-birnessite, causing a reduction in the peak intensity ratio between the (001) and (002) peaks from roughly 4:1 to 2:1 (Lopano et al. 2009). Rietveld refinement results for the exchange of Cs into hexagonal H-birnessite at pH 3, 5, 6.5, 9, and 10 are compiled in Table 1. Atom positions are listed in Table 2, and selected bond distances are listed in Table 3. A typical Rietveld refinement is shown in Figure 3 for Cs exchange into hexagonal H-birnessite.

All unit-cell parameters increased with extent of reaction, resulting in an increase of unit-cell volume with time. In order to determine the rate constant associated with the first stage of exchange (k_1), we fit the unit-cell volume as a function of time using Eqn. 8 (Fig. 4). To determine the initial rate of cation exchange for a given pH, we applied Eqn. 13, and the results of this analysis are presented in Table 4.

The dependence of the initial reaction rate on pH (Eqn. 14, Fig. 5) refined as

Revision 2.

240 $$\log\left(\frac{dV}{dt}\right) = -0.0791(pH) - 0.9885 \qquad R^2 = 0.894, \qquad (16)$$

241 which can be simplified to an exponential form where the initial rate constant, *w*, is the
242 coefficient and the reaction order, *n*, is the exponent:

243 $$\frac{dV}{dt} = 0.103\left[H^+\right]^{0.079}. \qquad (17)$$

244 As can be seen in Figure 5, the exchange rate of Cs^+ into the interlayer of hexagonal H-birnessite
245 decreased only slightly as the pH increased. By extension, the reaction order of the cation
246 exchange was also extremely small (0.079), indicating a weak dependence of exchange rate on
247 pH.

248 The change in final unit-cell volume increased as pH increased (Fig. 6), particularly as
249 pH exceeded 6. To the extent that unit-cell volume is a proxy for Cs^+ exchange, we can infer
250 that more Cs^+ is exchanged into the interlayer of hexagonal H-birnessite with increasing
251 alkalinity, consistent with the results of Chitrakar et al. (2011). The occupancy factor of the
252 interlayer cation also increased as pH increased from 3 to 10, which is direct evidence that more
253 Cs exchanged into the interlayer (Table 2). We tested this conclusion by ICP-MS analysis of Cs
254 and Mn in the eluate, which was collected as a function of time after it interacted with the
255 hexagonal H-birnessite. When pH was 6.5 or higher, all of the Cs was sequestered by the
256 birnessite powder in the first reaction stages. In Figure 7, we present the percentage of Cs
257 removed from or released to the flow-through solution as a function of time. Positive data points
258 indicate sequestration by the solid, whereas negative data points represent release of Cs by the
259 solid. For example, if an eluted aliquot collected at a given time was measured as 0.5 mM Cs,
260 then that represents +50 wt% sequestration (removal of Cs from the solution), since the flow-
261 through solution enters the capillary with a concentration of 1.0 mM Cs. As can be seen in this

figure, a maximum of only 25 wt% of the Cs in the influent was adsorbed within the first 20 minutes at pH 3, whereas 100 wt% of the Cs was sequestered by the birnessite over the first 100 min at pH 10. For all pH values, the sequestration of Cs eventually was followed by the release of Cs to the solution.

DISCUSSION

Controls of Cs uptake

We postulate that the rate and amount of Cs^+ uptake as a function of pH are controlled by two factors: 1) the charge on the octahedral sheets; and 2) the presence of competing cations (including H^+) in solution. The point-of-zero charge (PZC) of birnessite is approximately 3.0 (Tan et al. 2008), and the octahedral MnO_6 sheets thus become more negatively charged as pH increases beyond 3 (Murray 1974; McKenzie 1981). In order to maintain neutrality of the surface charge at high pH, more Cs must adsorb to surface sites. Thus, the change in surface charge as a function of pH may explain the increased uptake of Cs in more alkaline solutions.

Secondly, Cs exchange at low pH is not chemically favorable because, by Le Châtelier's principle, the excess number of protons in the starting solution drives the reaction in the reverse direction and prevents Cs cation exchange:

$$\text{H-birnessite}_{(s)} + Cs^+_{(aq)} \rightarrow \text{Cs-birnessite}_{(s)} + H^+_{(aq)}. \quad (18)$$

Finally, acidic dissolution occurs at a pH as low as 3 (Murray 1974; Eary and Ral 1987), and that may inhibit Cs from entering the interlayer due to $Mn^{2+}_{(aq)}$ production, where

$$MnO_{2(s)} + 2H^+_{(aq)} \rightarrow Mn^{2+}_{(aq)} + H_2O_{(l)} + \tfrac{1}{2}O_{2(g)}. \quad (19)$$

Measurements of the dissolved Mn in the leachate solutions from our experiments suggest that some dissolution did occur in the earliest stages of reaction (Fig. 8). At each pH, a small amount

of Mn desorbed or dissolved from the hexagonal H-birnessite, with the greatest measured value (5 ppm after 20 min) occurring at pH 6.5. At pH 3 (Fig. 8A), the initial release of Mn reached only 1 ppm, but unlike reactions at higher pH, the concentration of Mn in the leachate achieved a non-zero steady state concentration of approximately 200 ppb for the remainder of the reaction, indicating a constant loss of Mn^{2+} from the solid. This observation supports our inference that reductive dissolution of hexagonal H-birnessite occurs at low pH as Cs is exchanged into the interlayer, or perhaps a small amount of interlayer Mn^{2+} is forced into solution due to the large size of the incoming Cs^{+}.

Transformation from hexagonal to triclinic symmetry

Although we successfully refined all of the exchanged Cs-birnessite structures within the hexagonal *P -3* space group, we nevertheless speculate that the higher loading of Cs within birnessite at higher pH was promoted by a transformation towards triclinic symmetry. At pH 9 and 10, the occupancy of octahedral Mn increased from approximately 0.7 to 1.0 (Fig. 9), indicating that the concentration of octahedral vacancies dropped to zero with higher pH. As described in Silvester et al. (1997) and Post et al. (2008), vacancies in the octahedral sheet are a defining feature of hexagonal birnessite, whereas the absence of these vacancies is more representative of triclinic birnessite (Post et al. 2002). At the same time, there is a slight decrease in interlayer Mn^{2+} site occupancy from 0.17 to 0. It is possible that interlayer Mn is migrating from the interlayer into the octahedral sheet and it may be that Cs exchange into the interlayer promotes the transfer of Mn into the octahedral sheet due to the size and charge of Cs, which leads to the expansion of the interlayer.

Another indication that a symmetry transition was initiated at higher pH can be seen in the sharp increase in the change of unit-cell volume above pH 6 (Fig. 6). The unit-cell volume of triclinic M-birnessite is greater than that of hexagonal M-birnessite, and thus a hexagonal-triclinic structure transition would be accompanied by a step increase in unit-cell volume. Indeed, when the unit-cell volume behaviors are considered for each pH (Fig. 4), the low pH reactions exhibited a different character than those at high pH. For pH 6.5 and lower, one can clearly detect the two stages of reaction as modeled by Lopano et al. (2009) as two distinct regions with different slopes for *dV/dt*. Like Lopano et al. (2009), we interpret the abrupt increase in unit-cell volume in the first stage as representing the full exchange of Cs^+ for H^+; the comparatively lengthy second stage of minor volume increase reflects a positional ordering of Cs^+ within the interlayer. At pH 9 and 10, however, the dependence of the volume change is less easily demarcated into two regimes, perhaps because the exchange of Cs^+ continued long after the time that exchange had ceased in the experiments at low pH. Our analyses of the eluate strongly support this conclusion (Fig. 7). Consequently, the two-stages observed at low pH were blurred at high pH by the expansion of the interlayer and increased Cs^+ uptake. We attempted to refine the higher pH powders with a triclinic structure but the goodness of fit parameters became much worse than with a hexagonal structure.

Back reaction

The release of Cs following its uptake was observed at each pH, and that phenomenon requires some explanation. If Cs leached out of the interlayer, we would expect to see the unit-cell volume decrease towards the initial volume of hexagonal H-birnessite. However, in all instances the unit-cell volume remained constant once cation exchange was complete, indicating

that Cs remained in the interlayer. Rather, we speculate that Cs was released from edge or surface sites on the birnessite platelets, or as a result of the reordering of interlayer cations during stage two of the reaction. We recognize that some percentage of Cs is adsorbed rather than exchanged; indeed, studies such as that by Peacock and Sherman (2007) have demonstrated that the sorption of dissolved Ni^{2+} on the birnessite surface increases markedly from pH 1 to 7. However, our XRD data did not allow us to distinguish between exchanged and sorbed populations of Cs.

Mechanism of exchange

Cation exchange in layered structures conventionally has been explained through simple diffusion of solvated ions into the solid accompanied by counter-diffusion of cations from the solid to the solution (Helfferich 1962). If this mechanism is operative when Cs^{+} exchanges into hexagonal H-birnessite, then a Cs-rich reaction rim would form around the edges of each partially-exchanged birnessite grain as the Cs migrated from the edges of the grain towards the core until exchange was complete. Alternatively, Putnis (2002) has demonstrated that cation exchange commonly involves dissolution of the starting structure followed by reprecipitation of the final structure. This model also may create reaction rims, if the reprecipitation is pseudomorphic (Labotka et al. 2004), or it may be marked by the transient co-existence of endmember phases. In the present experiment, this mechanism would generate the growth of hexagonal Cs-birnessite particles at the expense of hexagonal H-birnessite.

The octahedral sheets in birnessite have the capacity to separate into monolayers when intercalated with organic ions and washed, and the monolayers then reconstruct as stacked crystals upon drying (Liu et al. 2000; Yang et al. 2004). By extension, Lopano et al. (2009)

proposed a "delamination-reassembly" mechanism for the substitution of Cs into triclinic Na-birnessite, and this exchange model represents a hybrid between simple diffusion and dissolution-reprecipitation. If this model is applied to the present system, adjacent octahedral sheets delaminated, allowing Cs cations to exchange with all of the protons within a single interlayer. Cation exchange then proceeded through a layer-by-layer substitution until all protons swapped out for Cs.

If this mechanism occurred during our experiments, then elemental maps of individual platelets of partially exchanged H-birnessite crystals would not exhibit a reaction rim. Instead, they would display a homogeneous distribution of Cs across a given grain. As can be seen in our ASEM elemental maps of partially exchanged hexagonal H-birnessite at pH 9 (Fig. 10), no Cs-rich reaction rims enveloped individual grains of birnessite. Consequently, we rule out diffusion as the exchange mechanism. Likewise, we do not believe that dissolution-reprecipitation was the exchange mechanism because there were no Cs-rich grains interspersed with Cs-depleted grains. Rather, the homogeneous distribution of Cs supports delamination-reassembly as the driving mechanism for exchange.

ACKNOWEDGEMENTS

Special thanks to Peter Eng and Nancy Lazarz at APS. Funding for this research was provided by the NSF-DOE Center for Environmental Kinetics Analysis (CEKA) Grant No. CHE-0431328 and NSF Grant No. EAR07-45374 and EAR11-47728. Use of the Advanced Photon Source was supported by the U. S. Department of Energy, Office of Science, Office of Basic Energy Sciences, under Contract No. DE-AC02-06CH11357.

Revision 2.

REFERENCES

Al-Attar, L., Dyer, A., Paajanen, A., and Harjula, R. (2003) Purification of nuclear wastes by novel inorganic ion exchangers. Journal of Materials Chemistry, 13(12), 2969-2974.

Barnett, M.O., Jardine, P.M., and Brooks, S.C. (2002) U(VI) adsorption to heterogeneous subsurface media: Application of a surface complexation model. Environmental Science & Technology, 36(5), 937-942.

Chitrakar, R., Makita, Y., and Sonoda, A. (2011) Cesium ion exchange on synthetic birnessite ($Na_{0.35}MnO_2 \cdot 0.6H_2O$). Chemistry Letters, 40, 1118-1120.

Denton, A.R., and Ashcroft, N.W. (1991) Vegard's law. Physical Review A, 43(6), 3161.

Dyer, A., Pillinger, M., Harjula, R., and Amin, S. (2000) Sorption characteristics of radionuclides on synthetic birnessite-type layered manganese oxides. Journal of Materials Chemistry, 10(8), 1867-1874.

Eary, L.E., and Ral, D. (1987) Kinetics of chromium (III) oxidation to chromium (VI) by reaction with manganese dioxide. Environmental Science & Technology, 21, 1187-1193.

Finger, L.W., Cox, D.E., and Jephcoat, A.P. (1994) A Correction for Powder Diffraction Peak Asymmetry Due to Axial Divergence. Journal of Applied Crystallography, 27, 892-900.

Fredrickson, J.K., Zachara, J.M., Kennedy, D.W., Kukkadapu, R.K., McKinley, J.P., Heald, S.M., Liu, C., and Plymale, A.E. (2004) Reduction of TcO4- by sediment-associated biogenic Fe(II). Geochimica et Cosmochimica Acta, 68(15), 3171-3187.

Fromherz, H. (1964) Physico-chemical calculations in science and industry. Butterworth & Co., London.

Fu, G., Allen, H.E., and Cowan, C.E. (1991) Adsorption of cadmium and copper by manganese oxide. Soil Science, 152(2), 72-81.

399 Gee, G.W., Oostrom, M., Freshley, M.D., Rockhold, M.L., and Zachara, J.M. (2007) Hanford
400 site vadose zone studies: An overview. Vadose Zone Journal, 6(4), 899-905.
401 Golden, D.C., Chen, C.C., and Dixon, J.B. (1986a) Synthesis of Todorokite. Science, 231(4739),
402 717-719.
403 Golden, D.C., Dixon, J.B., and Chen, C.C. (1986b) Ion exchange, thermal transformations, and
404 oxidizing properties of birnessite. Clays and Clay Minerals, 34(5), 511-520.
405 Heaney, P.J., Post, J.E., Lopano, C.L., and Hanson, J.C. (2003) Hydrogen exchange in Na-
406 birnessite: A time-resolved synchrotron X-ray diffraction analysis. Geological Society of
407 America Abstracts with Programs, 35, 620.
408 Helfferich, F. (1962) Ion Exchange. 624 p. McGraw-Hill, New York.
409 Labotka, T.C., Cole, D.R., Fayek, M., Riciputi, L.R., and Stadermann, F.J. (2004) Coupled
410 cation and oxygen-isotope exchange between alkali feldspar and aqueous chloride
411 solution. American Mineralogist, 89(11-12), 1822-1825.
412 Lanson, B., Drits, V.A., Feng, Q., and Manceau, A. (2002) Structure of synthetic Na-birnessite:
413 Evidence for a triclinic one-layer unit cell. American Mineralogist, 87(11-12), 1662-
414 1671.
415 Lanson, B., Drits, V.A., Silvester, E., and Manceau, A. (2000) Structure of H-exchanged
416 hexagonal birnessite and its mechanism of formation from Na-rich monoclinic buserite at
417 low pH. American Mineralogist, 85(5-6), 826-838.
418 Larson, A.C., and Von Dreele, R.B., 1994. GSAS-General Structure Analysis System. Los
419 Alamos National Laboratory,

Revision 2.

Lasaga, A.C. (1981) Rate Laws of Chemical Reactions. In A.C. Lasaga, and R.J. Kirkpatrick, Eds. Kinetics of Geochemical Processes, 8, p. 1-68. Mineralogical Society of America, Chelsea, MI.

Lindsey, K.A., and Gaylord, D.R. (1990) Lithofacies and sedimentology of the Miocene-Pliocene Ringold Formation, Hanford Site, South-Central Washington. Northwest Science, 64(3), 165-180.

Liu, Z., Ooi, K., Kanoh, H., Tang, W., and Tomida, T. (2000) Swelling and delamination behaviors of birnessite-type manganese oxide by intercalation of tetraalkylammonium ions. Langmuir, 16(9), 4154-4164.

Liu, Z.H., Kang, L.P., Zhao, M.Z., and Ooi, K. (2007) Preparation, ion-exchange, and electrochemical behavior of Cs-type manganese oxides with a novel hexagonal-like morphology. Journal of Materials Research, 22(9), 2437-2447.

Lopano, C.L., Heaney, P.J., Bandstra, J.Z., Post, J.E., and Brantley, S.L. (2011) Kinetic analysis of cation exchange in birnessite using time-resolved synchrotron X-ray diffraction. Geochimica Et Cosmochimica Acta, 75(14), 3973-3981.

Lopano, C.L., Heaney, P.J., and Post, J.E. (2009) Cs-exchange in birnessite: Reaction mechanisms inferred from time-resolved X-ray diffraction and transmission electron microscopy. American Mineralogist, 94(5-6), 816-826.

Lopano, C.L., Heaney, P.J., Post, J.E., Hanson, J., and Komarneni, S. (2007) Time-resolved structural analysis of K- and Ba-exchange reactions with synthetic Na-birnessite using synchrotron X-ray diffraction. American Mineralogist, 92(2-3), 380-387.

McKenzie, R.M. (1981) The surface charge on manganese dioxides. Australian Journal of Soil Research, 19, 41-50.

Revision 2.

McKinley, J.P., Zeissler, C.J., Zachara, J.M., Serne, R.J., Lindstrom, R.M., Schaef, H.T., and Orr, R.D. (2001) Distribution and retention of Cs-137 in sediments at the Hanford Site, Washington. Environmental Science & Technology, 35(17), 3433-3441.

Mikhail, E.M., and Misak, N.Z. (1988) Sorption of Cesium and Cobalt Radionuclides on a New Manganese Oxide. Applied Radiation and Isotopes, 39(11), 1121-1124.

Murray, J.W. (1974) The surface chemistry of hydrous manganese dioxide. Journal of Colloid and Interface Science, 46(3), 357-371.

Negra, C., Ross, D.S., and Lanzirotti, A. (2005) Soil manganese oxides and trace metals: Competitive sorption and microfocused synchrotron X-ray fluorescence mapping. Soil Science Society of America Journal, 69(2), 353-361.

O'Reilly, S.E., and Hochella, M.F. (2003) Lead sorption efficiencies of natural and synthetic Mn and Fe-oxides. Geochimica Et Cosmochimica Acta, 67(23), 4471-4487.

Peacock, C.L. and Sherman, D.M. (2007) Sorption of Ni by birnessite: Equilibrium controls on Ni in seawater. Chemical Geology, 238, 94-106.

Post, J.E. and Bish, D.L. (1989) Rietveld refinement of crystal structures using powder X-ray diffraction data. Reviews in Mineralogy, 20, 277-308.

Post, J.E., Heaney, P.J., and Ertl, A. (2008) Rietveld refinement of the rancieite structure using synchrotron powder diffraction data. Powder Diffraction, 23(1), 10-14.

Post, J.E., Heaney, P.J., and Hanson, J. (2002) Rietveld refinement of a triclinic structure for synthetic Na-birnessite using synchrotron powder diffraction data. Powder Diffraction, 17(3), 218-221.

Putnis, A. (2002) Mineral replacement reactions: from macroscopic observations to microscopic mechanisms. Mineralogical Magazine, 66(5), 689-708.

Revision 2.

Rietveld, H.M. (1969) A Profile Refinement Method for Nuclear and Magnetic Structures. Journal of Applied Crystallography, 2, 65-71.

Santelli, C.M., Webb, S.M., Dohnalkova, A.C., and Hansel, C.M. (2011) Diversity of Mn oxides produced by Mn(II)-oxidizing fungi. Geochimica Et Cosmochimica Acta, 75(10), 2762-2776.

Silvester, E., Manceau, A., and Drits, V.A. (1997) Structure of synthetic monoclinic Na-rich birnessite and hexagonal birnessite. 2. Results from chemical studies and EXAFS spectroscopy. American Mineralogist, 82(9-10), 962-978.

Stephens, P.W. (1999) Phenomenological model of anisotropic peak broadening in powder diffraction. Journal of Applied Crystallography, 32, 281-289.

Tan, H., Zhang, G.X., Heaney, P.J., Webb, S.M., and Burgos, W.D. (2010) Characterization of manganese oxide precipitates from Appalachian coal mine drainage treatment systems. Applied Geochemistry, 25(3), 389-399.

Tan, W.F., Lu, S.J., Liu, F., Feng, X.H., He, J.Z., and Koopall, L.K. (2008) Determination of the point-of-zero, charge of manganese oxides with different methods including an improved salt titration method. Soil Science, 173(4), 277-286.

Taylor, R.M., McKenzie, R.M., and Norrish, K. (1964) The mineralogy and chemistry of manganese in some Australian soils. Australian Journal of Soil Research, 2, 235-248.

Thompson, P., Cox, D.E., and Hastings, J.B. (1987) Rietveld Refinement of Debye-Scherrer Synchrotron X-Ray Data from Al2O3. Journal of Applied Crystallography, 20, 79-83.

Toby, B.H. (2001) EXPGUI, a graphical user interface for GSAS. Journal of Applied Crystallography, 34, 210-213.

Vaniman, D.T., Chipera, S.J., Bish, D.L., Duff, M.C., and Hunter, D.B. (2002) Crystal chemistry of clay-Mn oxide associations in soils, fractures, and matrix of the Bandelier Tuff, Pajarito Mesa, New Mexico. Geochimica Et Cosmochimica Acta, 66(8), 1349-1374.

Violante, A., and Pigna, M. (2002) Competitive sorption of arsenate and phosphate on different clay minerals and soils. Soil Science Society of America Journal, 66(6), 1788-1796.

Wall, A.J., Heaney, P.J., Mathur, R., Post, J.E., Hanson, J.C., and Eng, P.J. (2011) A flow-through reaction cell that couples time-resolved X-ray diffraction with stable isotope analysis. Journal of Applied Crystallography, 44, 429-432.

Wan, J.M., Larsen, J.T., Tokunaga, T.K., and Zheng, Z.P. (2004) pH neutralization and zonation in alkaline-saline tank waste plumes. Environmental Science & Technology, 38(5), 1321-1329.

Weaver, R.M., and Hochella, M.F. (2003) The reactivity of seven Mn-oxides with Cr-aq(3+): A comparative analysis of a complex, aq environmentally important redox reaction. American Mineralogist, 88(11-12), 2016-2027.

Webb, S.M., Tebo, B.M., and Bargar, J.R. (2005) Structural characterization of biogenic Mn oxides produced in seawater by the marine bacillus sp strain SG-1. American Mineralogist, 90(8-9), 1342-1357.

Yang, X.J., Makita, Y., Liu, Z.H., Sakane, K., and Ooi, K. (2004) Structural characterization of self-assembled MnO2 nanosheets from birnessite manganese oxide single crystals. Chemistry of Materials, 16(26), 5581-5588.

Zhao, W., Feng, X., Tan, W., Liu, F., and Ding, S. (2009) Relation of lead adsorption on birnessites with different average oxidation states of manganese and release of Mn2+/H+/K+. Journal of Environmental Sciences, 21, 520-526.

Revision 2.

FIGURE CAPTIONS

Figure 1. A schematic of the two stage cation exchange reaction: stage one is the complete exchange of cations while stage two is the reordering of cations within the interlayer. The structures represent projections along the *a*-axis. Atomic color assignments: O (yellow), Mn^{4+} (pink), Mn^{2+} (pink, interlayer), H_3O^+ (green), and Cs/H_2O (blue).

Figure 2. Stacked TR-XRD patterns of hexagonal H-birnessite exchanged with 0.001 *M* Cs^+ at pH 10, with 2θ (°) along the *x*-axis, intensity along the *y*-axis, and time (min) along the *z*-axis where each pattern represents 5 min in time.

Figure 3. A typical Rietveld refinement of Cs exchange into hexagonal H-birnessite at pH 6.5. The black symbols represent the collected data, the green line represents the background, and the red line represents the modeled XRD pattern. Finally, the purple line represents the difference between the background and modeled pattern in comparison to the collected data.

Figure 4. Volume, *V*, ($Å^3$) plotted versus time (min) fit with Vegard's Law (Eqn. 8) with k_1 (min^{-1}) as the rate constant of reaction stage one and k_2 (min^{-1}) as the rate constant of reaction stage two at (a) pH 3, (b) pH 5, (c) pH 6.5, (d) pH 9, and (e) pH 10.

Figure 5. The log of the initial rate plotted as a function of pH. The change in initial cation exchange rate is weakly dependent on pH.

Figure 6. The change in volume ($Å^3$) versus time (min) versus pH. The unit-cell volume increases as pH increases.

Figure 7. Plots of Cs uptake (wt%) from the flow-through solution as a function of time. Positive percentages represent Cs uptake while negative percentages represent Cs release from the hexagonal birnessite. More Cs is sequestered by the hexagonal H-birnessite as the pH increases. Each plot represents a cation exchange reaction completed at a different pH: (a) pH 3, (b) pH 5, (c) pH 6.5, (d) pH 9, and (e) pH 10.

Figure 8. Plots of the Mn concentration (ppm) in the leachate as a function of time (min). Each plot represents a cation exchange reaction completed at a different pH: (a) pH 3, (b) pH 5, (c) pH 6.5, (d), pH 9, and (e) pH 10.

Figure 9. $Mn_{(oct)}$ site occupancy increases to 1.0 as pH increases, indicating the vacancies within the octahedral Mn-O sheet are filled with oxidized $Mn^{2/3+}$ from the interlayer.

Figure 10. ASEM elemental maps showing the distribution of Mn, O, and Cs on partially exchanged hexagonal H-birnessite at pH 9 (40 min).

TABLES

Table 1. Final Rietveld refinement parameters for end-member hexagonal H-birnessite exchanged with 0.001 *M* Cs^+ at various pHs.

	pH 3	pH 5	pH 6.5	pH 9	pH 10
Space group	$P\bar{3}$	$P\bar{3}$	$P\bar{3}$	$P\bar{3}$	$P\bar{3}$
Unit cell					
a = b (Å)	2.85090(4)	2.85054(3)	2.85844(3)	2.86977(1)	2.87725(3)
c (Å)	7.37897(9)	7.36808(2)	7.35841(9)	7.37082(7)	7.37601(6)
V ($Å^3$)	51.938(8)	51.848(9)	52.068(4)	52.570(4)	52.882(1)
Refinement					
No. of diffraction poin	1676	1676	1676	1676	1676
No. of reflections	27	29	29	27	21
Diffraction range (2θ)	3.9-37.303	3.9-37.303	3.9-37.303	3.9-37.303	3.9-37.303
No. of variables	32	31	32	31	30
$R(F^2)$	0.0193	0.017	0.0175	0.017	0.018
R_{wp}	0.0147	0.0105	0.0144	0.0195	0.0195
χ^2	4.823	3.788	3.941	3.473	2.756

562
563 Table 2. Atomic coordinates and isotropic displacement factors for Cs-exchanged hexagonal H-
564 birnessite across a wide pH range.
565

pH	Atom	x	y	z	Site occupancy factor	U_{iso} x 10^2 ($Å^2$)**
3	Mn_{oct}	0	0	0	0.738(4)	1.500
	O_{oct}	0.3333	0.6667	0.12145(1)	1.000	2.477
	O_{int}*	0.6667	0.3333	0.46085(9)	0.667(2)	8.000
	Mn_{int}	0	0	0.72346(9)	0.167(7)	1.500
5	Mn_{oct}	0	0	0	0.709(2)	1.500
	O_{oct}	0.3333	0.6667	0.11788(9)	1.000	2.477
	O_{int}*	0.6667	0.3333	0.46895(2)	0.682(0)	8.000
	Mn_{int}	0	0	0.72635(5)	0.179(0)	1.500
6.5	Mn_{oct}	0	0	0	0.816(5)	1.500
	O_{oct}	0.3333	0.6667	0.12060(1)	1.000	2.477
	O_{int}*	0.6667	0.3333	0.46532(5)	0.727(7)	8.000
	Mn_{int}	0	0	0.71783(1)	0.160(7)	1.500
9	Mn_{oct}	0	0	0	1.000(0)	1.500
	O_{oct}	0.3333	0.6667	0.10760(3)	1.000	2.477
	O_{int}*	0.6667	0.3333	0.45128(2)	0.879(1)	8.000
	Mn_{int}	0	0	0.69510(1)	0.000	1.500
10	Mn_{oct}	0	0	0	1.000(0)	1.500
	O_{oct}	0.3333	0.6667	0.10019(2)	1.000	2.477
	O_{int}*	0.6667	0.3333	0.44941(9)	0.892(8)	8.000
	Mn_{int}	0	0	0.68417(5)	0.000	1.500

566
567 *O_{int} designates a combined O (water) and Cs site.
568 **Values of U_{iso} were fixed.

Table 3. Selected bond distance values for Cs-exchanged hexagonal H-birnessite as a function of pH.

Bond	pH 3	pH 5	pH 6.5	pH 9	pH 10
Mn_{oct}-Mn_{oct}	2.85090(29) x 6	2.85054(32) x 6	2.85844(35) x 6	2.86977(32) x 6	2.87725(31) x 6
Mn_{oct}-O_{oct}	1.874(4) x 6	1.861(4) x 6	1.874(5) x 6	1.837(4) x 6	1.8182(34) x 6
O_{oct}-O_{int}	3.045(19) x 3	3.066(18) x 3	3.026(16) x 3	3.027(17) x 3	3.062(11) x 3
O_{oct}-O_{int}	3.074(18)	3.044(19)	3.047(23)	3.251(21)	3.317(19)
Mn_{int}-O_{oct}	2.005(5) x 3	2.006(4) x 3	2.034(6) x 3	2.205(10 x 3	2.300(12) x 3
Mn_{int}-O_{int}	2.542(16) x 3	2.511(15) x 3	2.485(19) x 3	2.444(18) x 3	2.400(17) x 3
Mn_{int}-O_{int}	2.135(13) x 3	2.186(14) x 3	2.131(13) x 3	1.977(12) x 3	1.931(12) x 3

575
576 Table 4. The first stage rate constant, k_1, and initial rate, dV/dt, of Cs^+ exchange into hexagonal
577 H-birnessite as a function of pH.
578

pH	k_1 **(min^{-1})**	dV/dt **($Å^3$/min)**
3	0.195 ± 0.0132	0.064 ± 0.0045
5	0.101 ± 0.0156	0.037 ± 0.0070
6.5	0.122 ± 0.0325	0.033 ± 0.0110
9	0.122 ± 0.2265	0.016 ± 0.0853
10	0.066 ± 0.0962	0.021 ± 0.1106

579
580
581
582

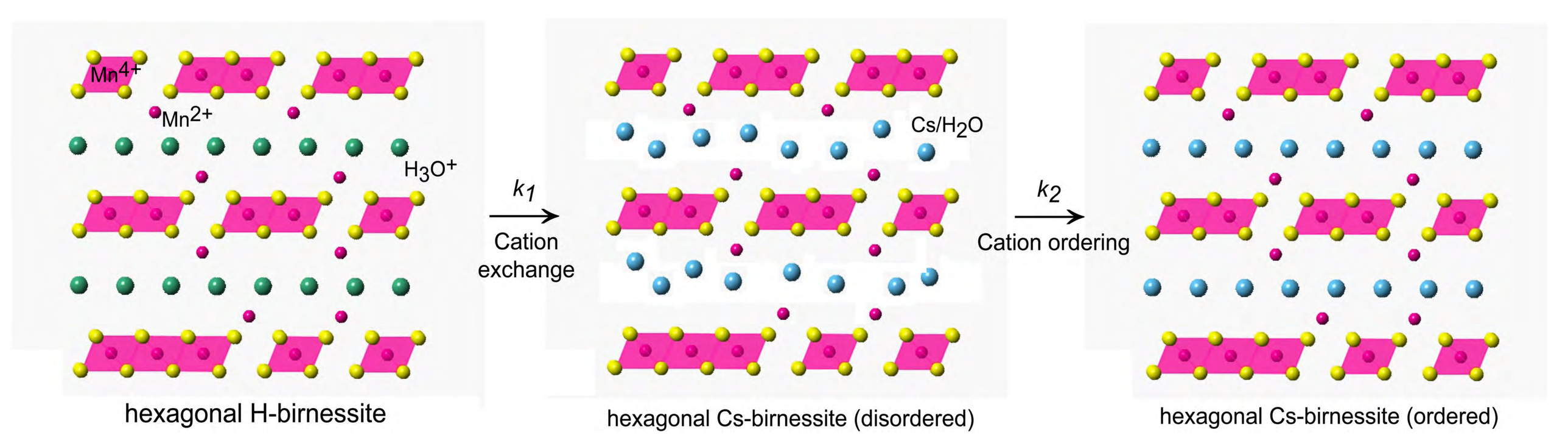
Mn4+
Mn2+
H3O+
k1
Cation exchange
Cs/H2O
k2
Cation ordering
hexagonal H-birnessite
hexagonal Cs-birnessite (disordered)
hexagonal Cs-birnessite (ordered)

a

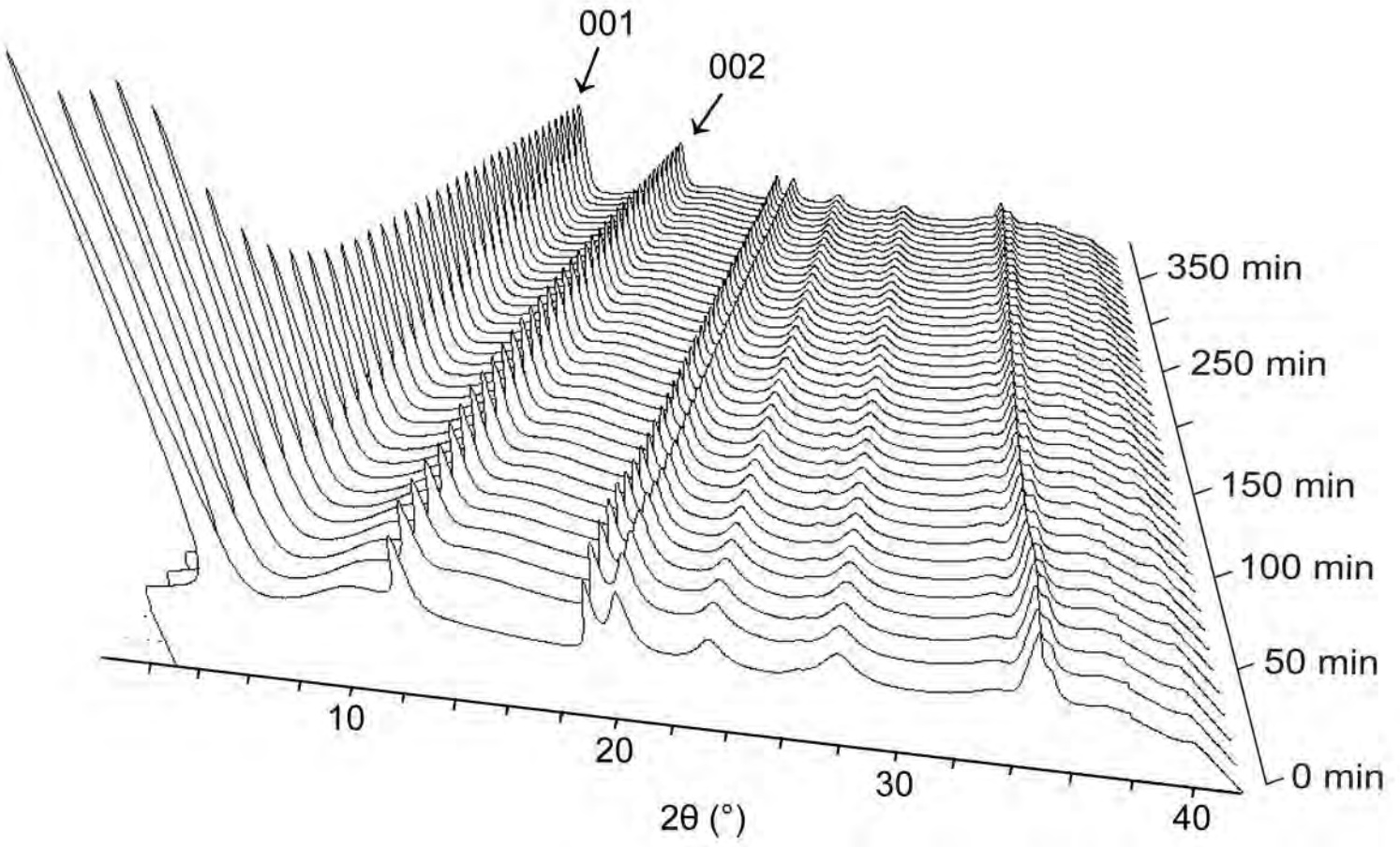

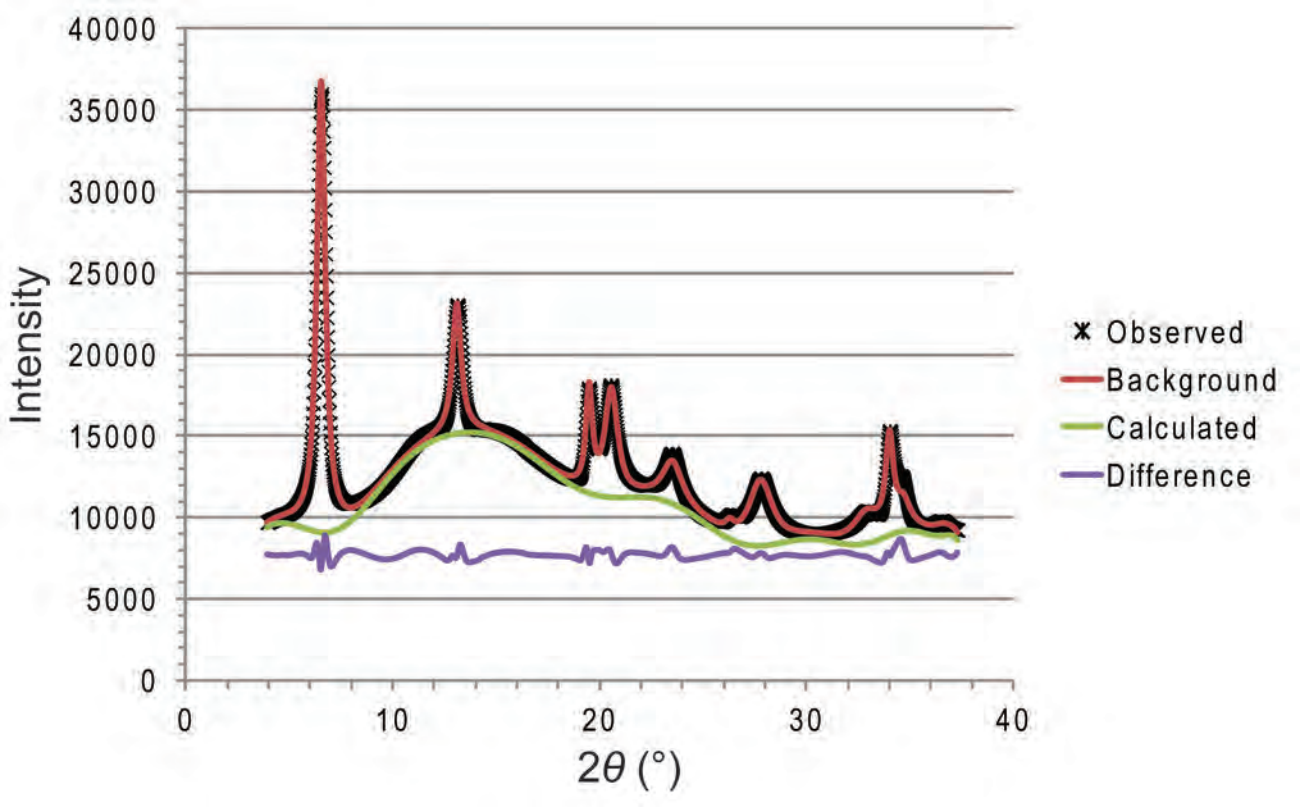
40000
35000
30000
25000
20000
15000
10000
5000
0
Intensity
0
10
20
30
40
2θ (°)
Observed
Background
Calculated
Difference

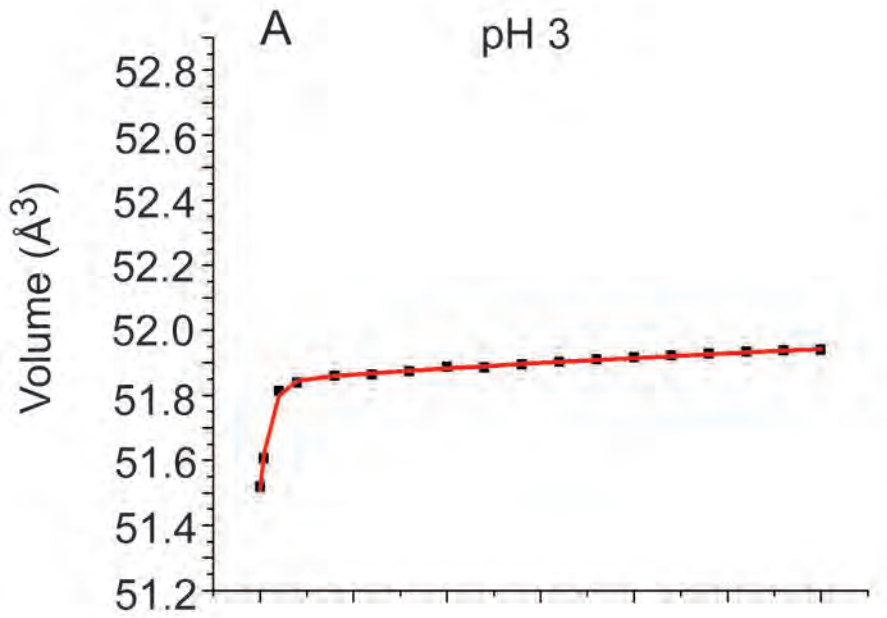
A
pH 3
Volume (Å3)
52.8
52.6
52.4
52.2
52.0
51.8
51.6
51.4
51.2

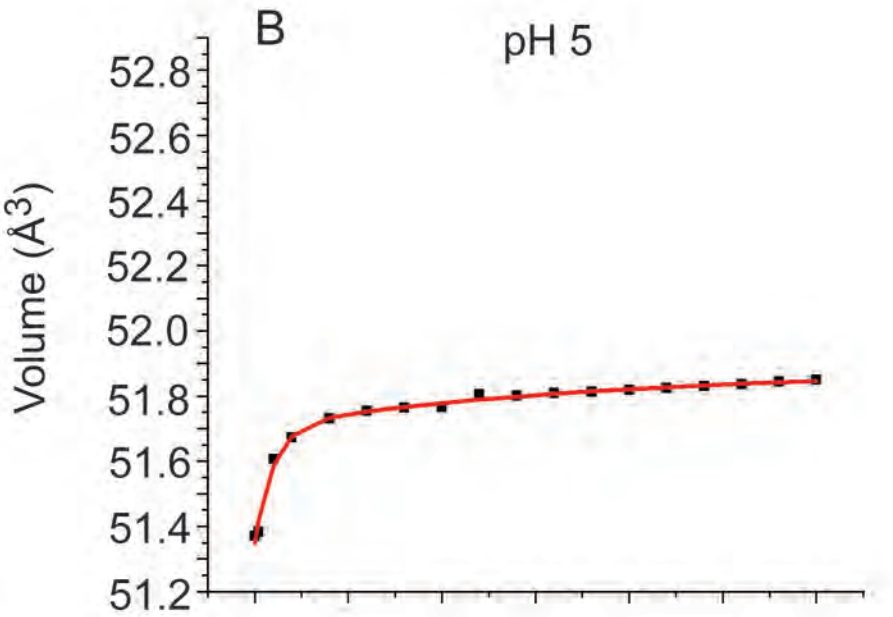
B
pH 5
Volume (Å3)
52.8
52.6
52.4
52.2
52.0
51.8
51.6
51.4
51.2

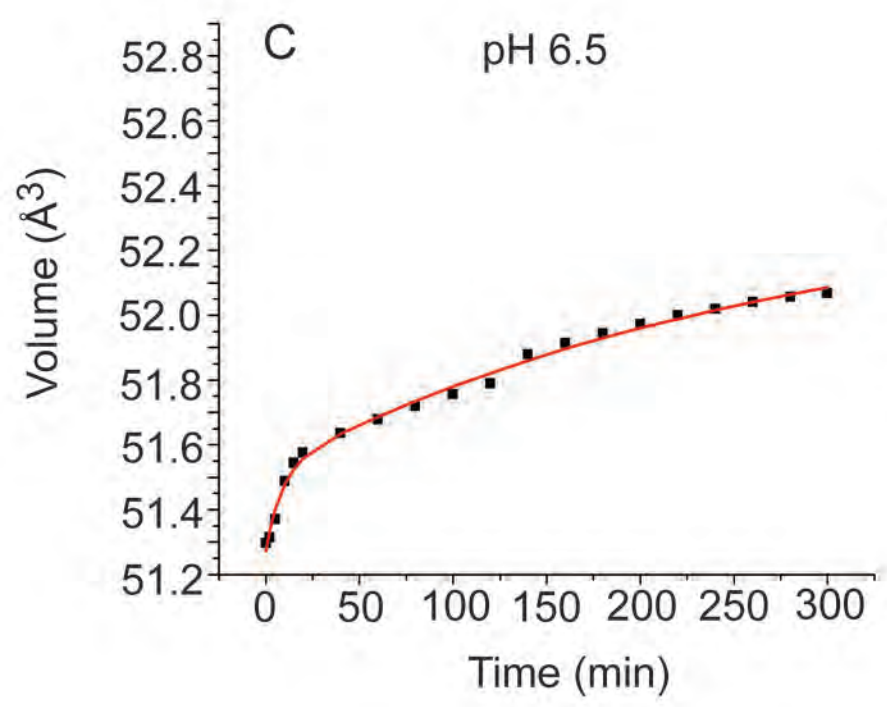
C
pH 6.5
Volume (Å3)
52.8
52.6
52.4
52.2
52.0
51.8
51.6
51.4
51.2
0
50
100
150
200
250
300
Time (min)

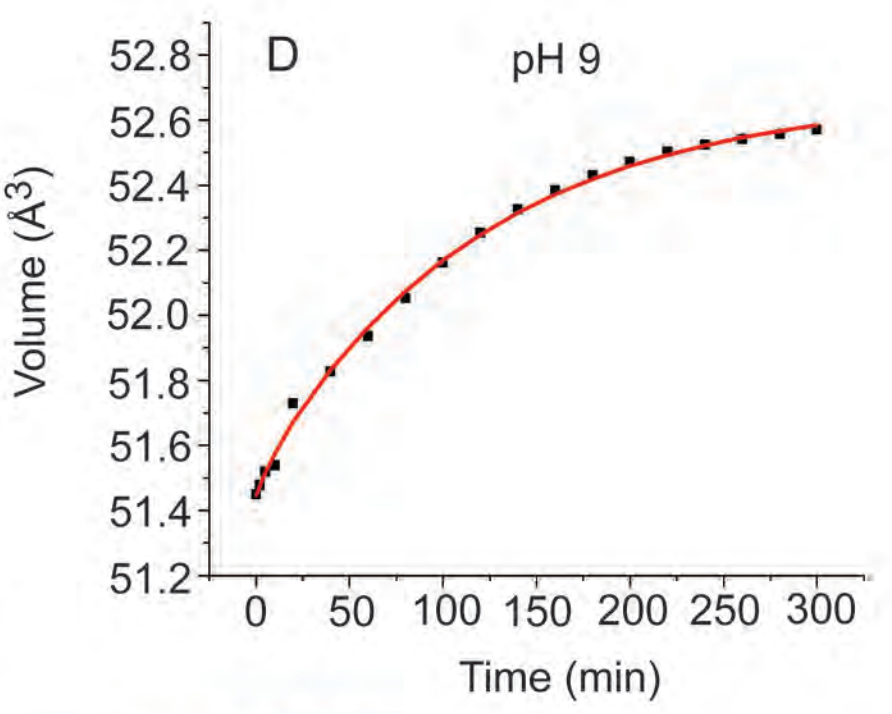
D
pH 9
Volume (Å3)
52.8
52.6
52.4
52.2
52.0
51.8
51.6
51.4
51.2
0
50
100
150
200
250
300
Time (min)

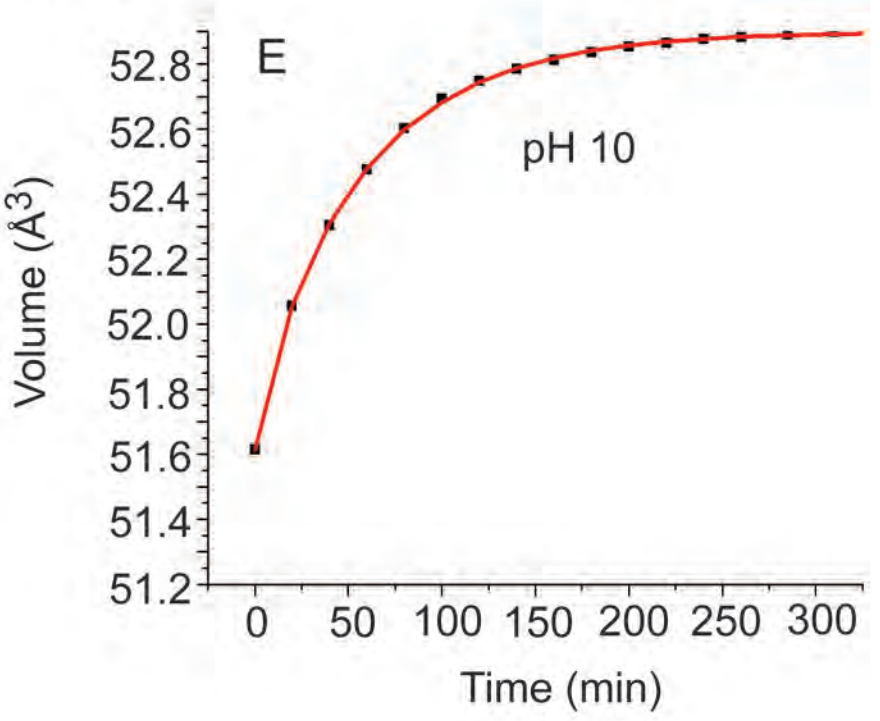
E
pH 10
Volume (Å3)
52.8
52.6
52.4
52.2
52.0
51.8
51.6
51.4
51.2
0
50
100
150
200
250
300
Time (min)

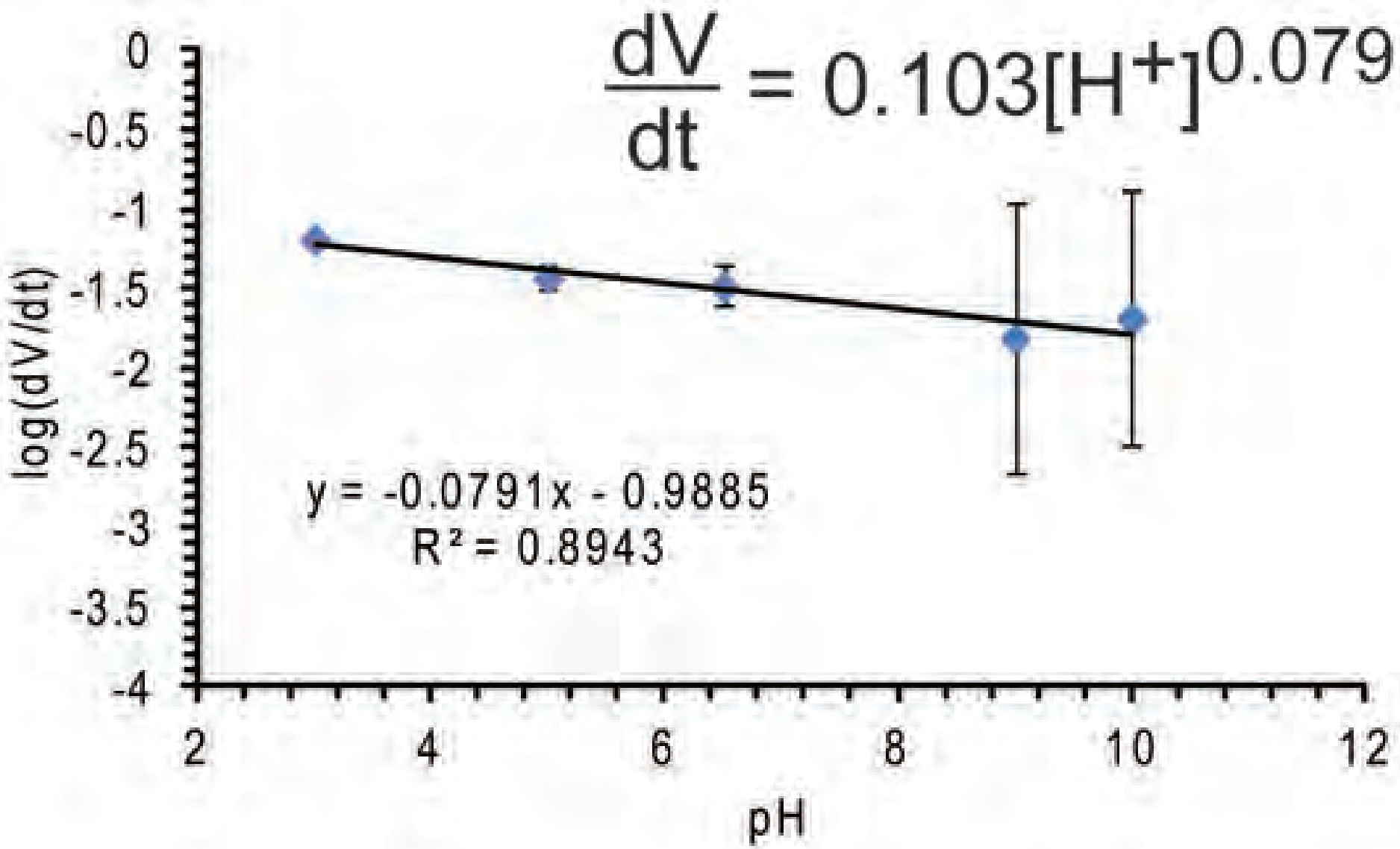
$\frac{dV}{dt} = 0.103[H^+]^{0.079}$
0
-0.5
-1
-1.5
-2
-2.5
-3
-3.5
-4
log(dV/dt)
y = -0.0791x - 0.9885
R² = 0.8943
2
4
6
8
10
12
pH

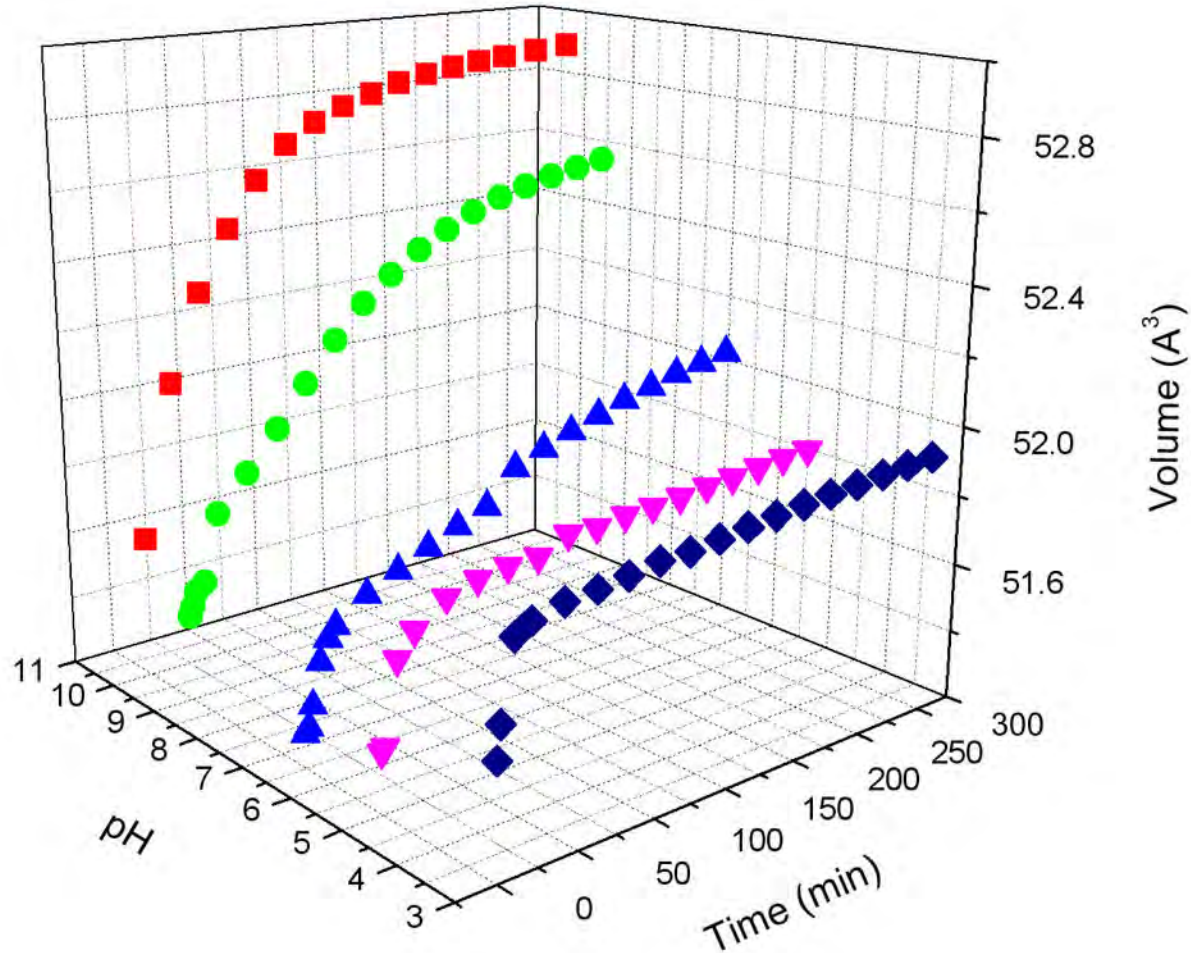
52.8
52.4
52.0
51.6
Volume (A3)
11
10
9
8
7
6
5
4
3
pH
0
50
100
150
200
250
300
Time (min)

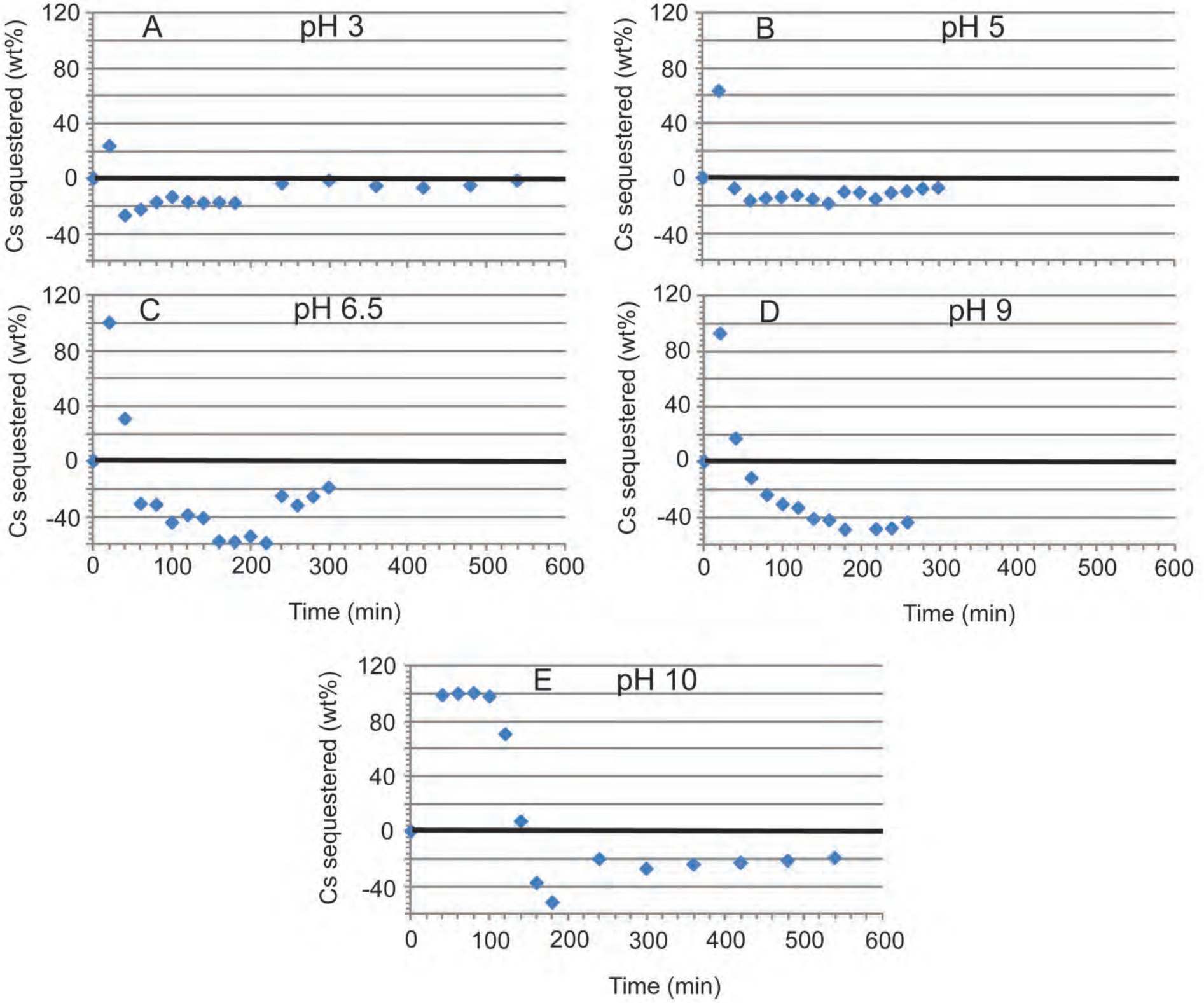
A
pH 3
B
pH 5
C
pH 6.5
D
pH 9
E
pH 10
Cs sequestered (wt%)
Time (min)
120
80
40
0
-40
0
100
200
300
400
500
600

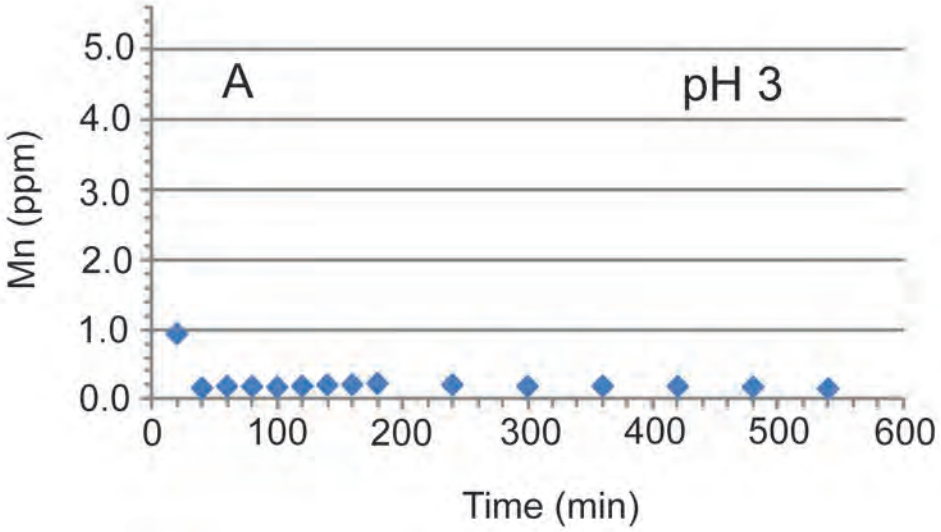
A
pH 3
Mn (ppm)
Time (min)
0.0
1.0
2.0
3.0
4.0
5.0
0
100
200
300
400
500
600

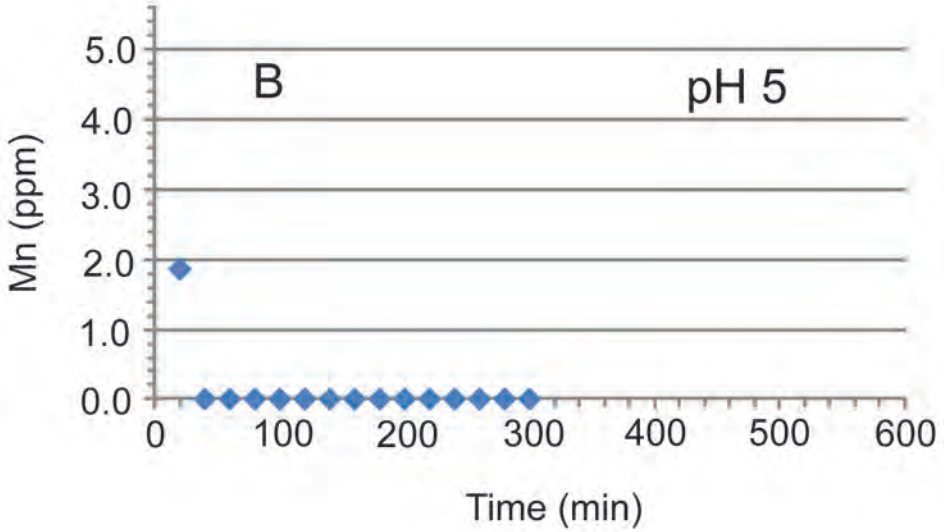
B
pH 5
Mn (ppm)
Time (min)
0.0
1.0
2.0
3.0
4.0
5.0
0
100
200
300
400
500
600

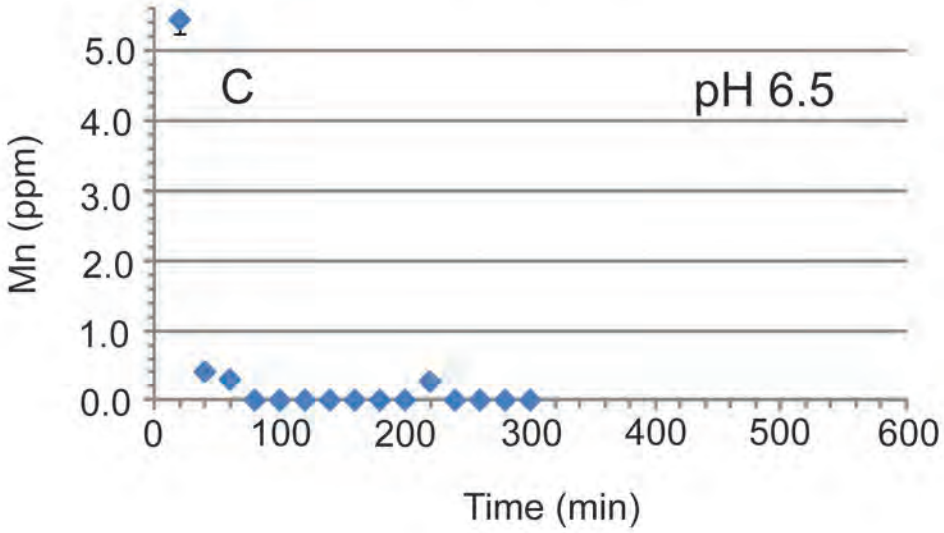
C
pH 6.5
Mn (ppm)
Time (min)
0.0
1.0
2.0
3.0
4.0
5.0
0
100
200
300
400
500
600

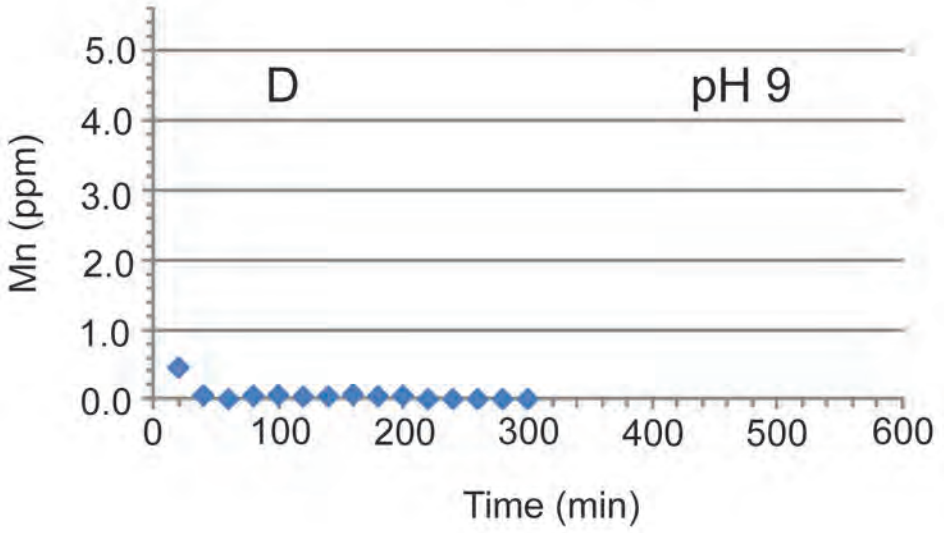
D
pH 9
Mn (ppm)
Time (min)
0.0
1.0
2.0
3.0
4.0
5.0
0
100
200
300
400
500
600

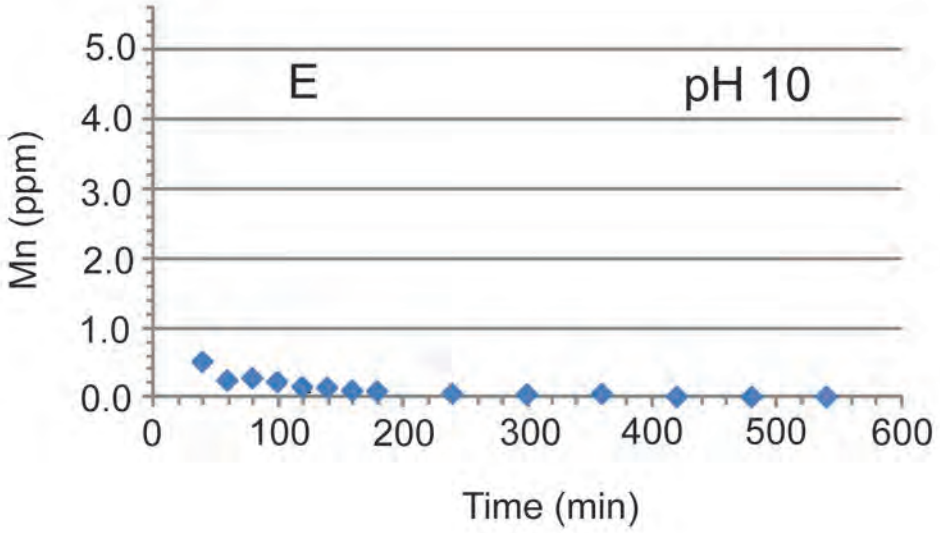
E
pH 10
Mn (ppm)
Time (min)
0.0
1.0
2.0
3.0
4.0
5.0
0
100
200
300
400
500
600

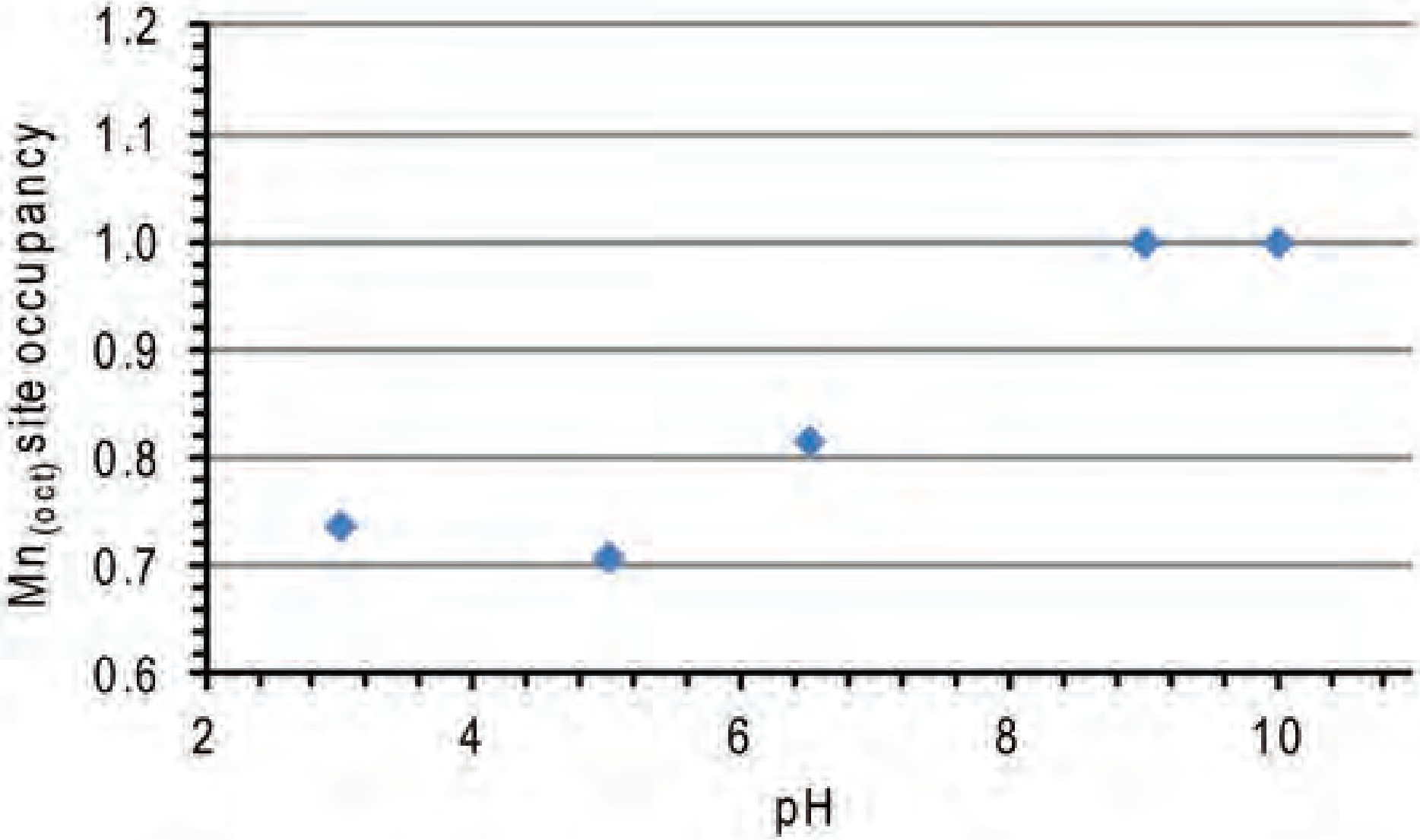
1.2
1.1
1.0
0.9
0.8
0.7
0.6
$Mn_{(oct)}$ site occupancy
2
4
6
8
10
pH

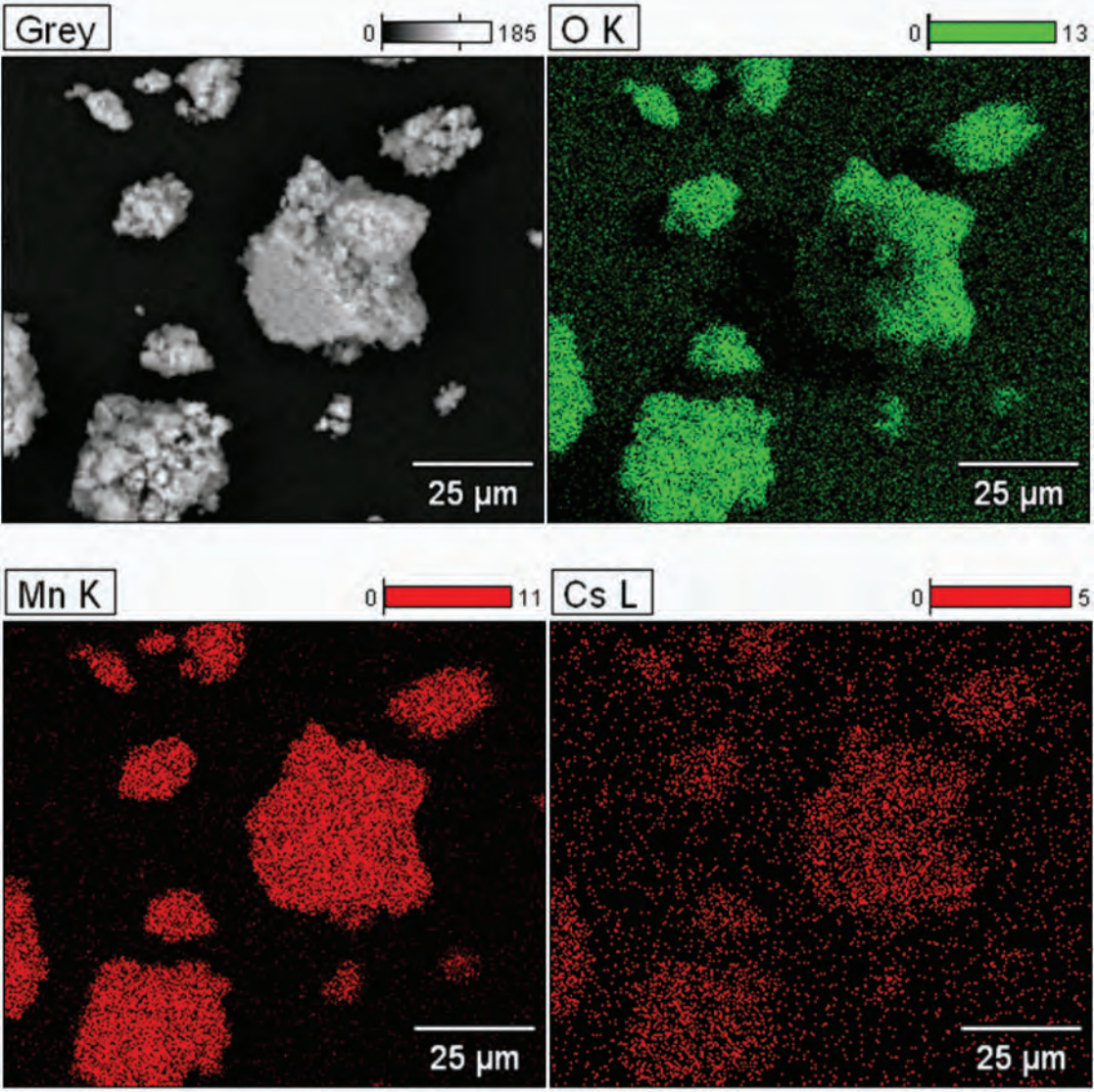
Grey
0
185
25 µm
O K
0
13
25 µm
Mn K
0
11
25 µm
Cs L
0
5
25 µm